ACS APPLIED MATERIALS & INTERFACES

Research Article

Cite This: ACS Appl. Mater. Interfaces 2018, 10, 28850−28859

www.acsami.org

Multiscale Functional Imaging of Interfaces through Atomic Force Microscopy Using Harmonic Mixing

Joseph L. Garrett,[†,‡] Marina S. Leite,[‡,§] and Jeremy N. Munday*[,‡,∥]

[†]Department of Physics, [‡]Institute for Research in Electronics and Applied Physics, [§]Department of Materials Science and Engineering, and [∥]Department of Electrical and Computer Engineering, University of Maryland, College Park, Maryland 20742, United States

Supporting Information

ABSTRACT: The spatial resolution of atomic force microscopy (AFM) needed to resolve material interfaces is limited by the tip−sample separation (d) dependence of the force used to record an image. Here, we present a new multiscale functional imaging technique that allows for in situ tunable spatial resolution, which can be applied to a wide range of inhomogeneous materials, devices, and interfaces. Our approach uses a multifrequency method to generate a signal whose d-dependence is controlled by mixing harmonics of the cantilever's oscillation with a modulated force. The spatial resolution of the resulting image is determined by the signal's d-dependence. Our measurements using harmonic mixing (HM) show that we can change the d-dependence of a force signal to improve spatial resolution by up to a factor of two compared to conventional methods. We demonstrate the technique with both Kelvin probe force microscopy (KPFM) and bimodal AFM to show its generality. Bimodal AFM with harmonic mixing actuation separates conservative from dissipative forces and is used to identify the regions of adhesive residue on exfoliated graphene. Our electrostatic measurements with open-loop KPFM demonstrate that multiple force modulations may be applied at once. Further, this method can be applied to any tip−sample force that can be modulated, for example, electrostatic, magnetic, and photoinduced forces, showing its universality. Because HM enables in situ switching between high sensitivity and high spatial resolution with any periodic driving force, we foresee this technique as a critical advancement for multiscale functional imaging.

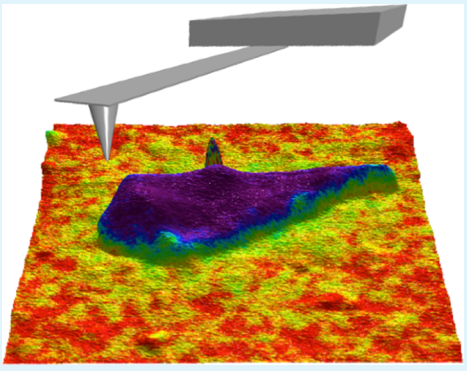

KEYWORDS: *functional imaging, scanning probe microscopy, Kelvin probe force microscopy, bimodal AFM, van der Waals materials*

INTRODUCTION

The development of atomic force microscopy (AFM) catalyzed much of the growth in nanoscience and nanotechnology over the past three decades.[1] In addition to imaging surface topography, it provided a basis for the development of additional scanning probe techniques that use AFM to control tip−sample separation, d, while also measuring functional material properties.[2−4] Even though Kelvin probe force microscopy (KPFM) was one of the first functional force microscopy techniques to be invented,[5−7] many recent improvements to the KPFM technique[8−12] have been motivated by the need to investigate emerging technologies at the nanoscale, including solar cells, batteries, catalysts, composites, two-dimensional (2D) materials, and biomolecular sensors.[13−24] Like many functional scanning probe methods, the spatial resolution of KPFM is significantly worse than the resolution achieved with topographical imaging. To mitigate the lower resolution of functional imaging, deconvolution procedures have been developed to identify the relative electrostatic potentials of different regions on a device or sample, which are assigned to particular topographical features.[25,26]

Although deconvolution procedures work well for determining the properties of homogeneous surfaces, they work less well at interfaces, where the shape of the potential change is often critical for determining macroscopic properties. Even worse, when spatial variations in material properties are not correlated with topographical differences, deconvolution methods are insufficient to characterize the surface of a sample because they lack a way to demarcate different regions. For example, metal surfaces contain small variations in the electrostatic potential at the nanoscale, called patch potentials. Because patch potentials are typically not correlated with topography, deconvolution methods do not improve how well they are resolved. Patch potentials are important to understanding decoherence in quantum computing, charge dynamics in 2D electronics and polymers, and artifacts in precision force measurements.[27−34] The autocorrelation function of a surface's potential quantifies the spatial distribution of the electric fields emanating from the patches. Because the spatial resolution of KPFM itself determines a lower bound to this autocorrelation

Received: May 16, 2018
Accepted: July 24, 2018
Published: August 16, 2018

DOI: 10.1021/acsami.8b08097
ACS Appl. Mater. Interfaces 2018, 10, 28850−28859

function, measurements of the surface potential at a single magnification cannot determine if the patches are being fully resolved. Indeed, our recent measurements showed that the force from patch potentials can be underestimated by at least an order of magnitude if imaged with insufficient spatial resolution, which motivated us to implement heterodyne (H-) KPFM rather than amplitude-modulation (AM) approaches.[33]

The spatial resolution of dynamic AFM is limited primarily by three factors:[35] tip geometry, jump-to-contact, and the dependence of the tip−sample interaction on the separation, d. The first two of these factors can be controlled by either the choice of cantilever (tip radius and spring constant) or scan parameters (drive amplitude and set point).[36,37] Few techniques have been used to control the signal's d-dependence in particular situations, and no general method has yet emerged. One successful approach to increase the d-dependence of the tip−sample force is to immerse a sample in liquid to minimize long-range forces.[38,39] However, operation in liquid lowers the cantilever Q-factor, and the environment may not be suitable for all samples. Another technique is to affix a dissimilar particle to the end of the tip apex,[40−42] but stability on rougher surfaces and in ambient conditions has not been tested. Other methods to increase the d-dependence of the signal include frequency modulation and phase detection, which, in the small-amplitude limit, detect the force gradient instead of the force itself to increase the d-dependence.[7] The paradigm of imaging force gradients, instead of forces, to improve spatial resolution has been further generalized into the sideband technique, which can be used with any force that can be driven at more than a few hundred hertz.[8,10,43−45] Imaging with the higher harmonics of cantilever oscillation has also been shown to improve resolution,[46] but the method is incompatible with functional imaging and, because these harmonics are not, in general, amplified by the resonances of the cantilever, noise masks the resolution improvement except at extremely slow scan speeds (≈4 nm/s).

Here, we demonstrate a general technique to control the spatial resolution of AFM imaging by modifying the power law of the distance dependence of the measured signal. This harmonic mixing (HM) method generalizes sideband actuation by taking advantage of the nonlinearity of the tip−surface interactions in order to modify the d-dependence of the detected signal. Using HM actuation with KPFM, we achieve a factor of two resolution enhancement compared to traditional methods. Further, we determine the detection bandwidth of HM with open-loop KPFM,[47−49] which relies on computing the ratio of two signals generated by the electrostatic force. Finally, we assess the capacity of HM to utilize forces other than the electrostatic force by modulating the total tip−sample force as in bimodal AFM,[50−52] where we find that actuating bimodal AFM with the HM technique separates conservative and dissipative forces without postprocessing. Our results reveal the potential of HM-AFM for the functional characterization of nanoscale systems, spanning from nanostructured solar cells to metallic building blocks for nanophotonics and 2D heterojunctions.

RESULTS AND DISCUSSION

HM-AFM Technique. In the HM technique, spatial resolution is controlled by choosing the d-dependence of the measured signal. This d-dependence is modified by mixing harmonics of the oscillation of the cantilever at one (carrier) frequency, ω_T, which is also used for the topography feedback loop, with force modulation at another frequency, ω_M, in order to excite cantilever oscillations, amplified by an eigenmode, at a third frequency, ω_D (see Figure 1). As in most dynamic AFM

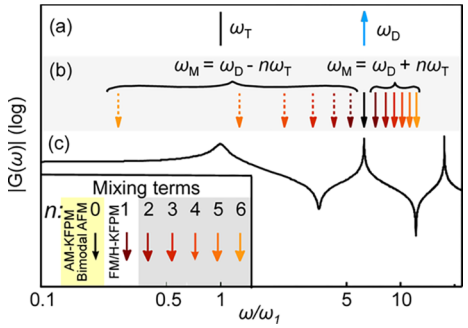

Figure 1. Applied and detected signals pictured above the cantilever transfer function as a function of frequency. (a) Frequencies for the carrier signal/topography control (ω_T, |) and signal detection (ω_D, blue arrow). (b) Different frequencies at which the force can be modulated to generate a signal at ω_D. The arrows showing distinct choices for ω_M are identified in the inset. Solid arrows correspond to "+", dashed arrows correspond to "−", and the colors correspond to different n. (c) Cantilever transfer function $G(\omega)$ used to amplify the signal at ω_D.

methods, the cantilever is oscillated at frequency ω_T, typically chosen to be at the first cantilever eigenmode, to maintain steady period-averaged tip−sample separation. The time dependence of a tip−sample force can then be approximated as a Taylor series around the average tip−sample separation. Because tip−sample forces are typically nonlinear, higher-n terms of the series have a more abrupt dependence on d than lower-n terms, where n indexes the series. The $n > 1$ terms excite higher harmonics in the cantilever's motion, but typically they are below the noise level except for very slow imaging because they do not generally coincide with cantilever resonance frequencies. By using a detection frequency, ω_D, near a cantilever resonance, HM enables detection of signals generated by higher-order terms of the Taylor series. After the frequencies ω_D and ω_T are chosen, the force modulation frequency is selected to satisfy $\omega_M = \omega_D \pm n\omega_T$. The choice of n then determines the d-dependence of the signal. For example, a signal generated by the electrostatic force follows a $d^{-(n+1)}$ power law when amplified by the nth term (see Figure 2 and Supporting Information). Note that $n = 0$ corresponds to traditional AM-KPFM, and $n = 1$ refers to frequency-modulated and H-KPFM (see the inset of Figure 1).

Because the HM technique relies on modifying a signal's d-dependence to control the spatial resolution, we first test its ability to effectively tailor this d-dependence. We apply an ac voltage to the probe and use the $F_{2\omega}$ force to drive oscillations at ω_D because it is insensitive to potential changes that would otherwise affect the magnitude of the generated signal.[53] Signal versus separation curves are plotted in Figure 2 for $n = 0$−3. The signals' d-dependence is found to roughly follow the predicted power laws, with $n = 0$ and 1 showing excess signal at large separations because of stray capacitance from the cantilever that is not included in the model (discussed below) and $n = 2$ and 3 showing excess signal at short separations. Because the signals follow the predicted d-dependences well, we calculate the resolutions assuming the ideal power laws (see the Supporting Information).

DOI: 10.1021/acsami.8b08097
ACS Appl. Mater. Interfaces 2018, 10, 28850−28859

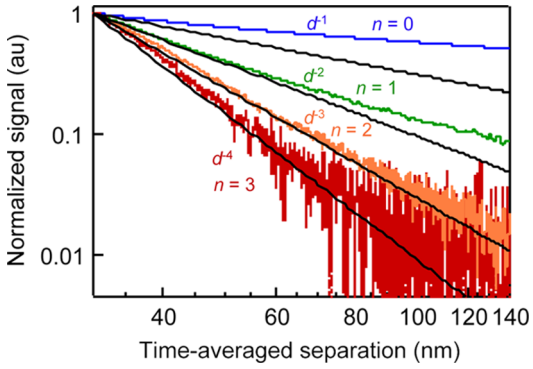

Figure 2. Power laws of the KPFM signals generated by mixing the electrostatic force with different harmonics n, shown here for the first four n as a function of separation for a 5 V driving voltage. When amplified by the nth term, the signal follows a $d^{-(n+1)}$ power law, shown for comparison (solid black lines).

We calculate the relationship between the d-dependence of a signal and the spatial resolution of an image acquired with that signal using the proximity force approximation (PFA). The PFA models the tip as a sphere of radius R, neglecting the tip−cone and cantilever, and posits that each small area of the tip interacts with the closest region of the sample. The total tip−sample force is found by integrating over the tip apex. To determine the spatial resolution of the signal, we model a potential boundary as a Heaviside step function (see the Supporting Information). The distance over which 80% of the force change occurs, that is, the 10−90 resolution (l_{10-90}), is used to define the spatial resolution. For $d \ll R$, the relationship between the resolutions achieved with signals that depend on $d^{-(n+1)}$ and d^{-n} is described by

$$l_{10-90}(d^{-(n+1)}) = \left(1 - \frac{1}{2n+1}\right) l_{10-90}(d^{-n}) \quad (1)$$

where the resolution is written as a function of its d-dependence (see eq S9). Equation 1 implies that the resolution can be improved arbitrarily by using large n, but with each increase of resolution, there is a simultaneous decrease of the driving force. For the electrostatic force, in the small amplitude Taylor series limit, the magnitude of the driving force decreases by (see the Supporting Information for derivation)

$$|F_{\omega_M \pm (n+1)\omega_T}| = \left(\frac{A_T}{2\bar{d}}\right) |F_{\omega_M \pm n\omega_T}| \quad (2)$$

where $F_{\omega_M \pm n\omega_T}$ is the component of the force driving the signal at $\omega_D = \omega_M \pm n\omega_T$, A_T is the amplitude of the oscillation at ω_T, and $\bar{d}$ is the time-averaged separation. Although the Taylor series approximation leads to a force that is proportional to A_T, a numerical analysis shows that there is an A_T that maximizes the signal (Figure S1) for a given n and closest approach. Scanning close to the surface damps the oscillation slightly, but changes to the transfer function, particularly higher eigenmodes, are small (Figure S2).

An alternative method for improving spatial resolution is to reduce the tip radius, R. In eq 2, increasing n by 1 reduces the actuating force, and hence the sensitivity, by about half. Because force is proportional to R in the PFA, increasing n by one has an effect on the sensitivity equivalent to halving R. Because the spatial resolution is proportional to $\sqrt{R}$ when d is much less than R, halving the radius leads to a 29% increase in spatial resolution.[10] The enhancement in spatial resolution due to increasing n is determined by eq 1, where the first few (cumulative) improvements are calculated to be 33, 47, 54%, and so on. Note that for small values of n, raising this quantity by one causes a change in both spatial resolution and sensitivity comparable to halving R. However, it is frequently inconvenient and sometimes not possible to change the probe (and, therefore, the radius of the tip used during scanning) in between measurements, as it requires unloading the cantilever, which could easily disrupt an experiment. In situ techniques to monitor or increase R work with many surfaces,[54] but techniques to reduce R are limited to certain substrates.[55] The radius of a metal-coated probe, typical for electrostatic measurements in air, is >20 nm. Thus, HM is competitive with, and in many situations preferable to, using a tip with a smaller R.

Measuring Spatial Resolution and Voltage Contrast. A flake of few-layer graphene (FLG) on a Si substrate is scanned with HM-KPFM (Figure 3). An ac voltage at frequency ω_M drives a cantilever oscillation and a feedback voltage is used to minimize it and to estimate the contact potential difference, V_{CPD}, as is typical for closed-loop KPFM.[6] The images presented in Figure 3 show a clear improvement in spatial resolution at higher n. A concomitant decrease in the signal-to-noise ratio is observed, resulting from the signal generation procedure that halves the driving force with each increase in n. Because it is necessary to image a boundary to a distance several times larger than the resolution in order to verify that the asymptotic limits of the potential are truly reached, interfaces allow the determination of resolution with less uncertainty than nanoparticles, although scans of nanoparticles do also show a resolution enhancement (Figure S3). To accurately determine the spatial resolution, we first determine the location of the two materials (FLG and Si)

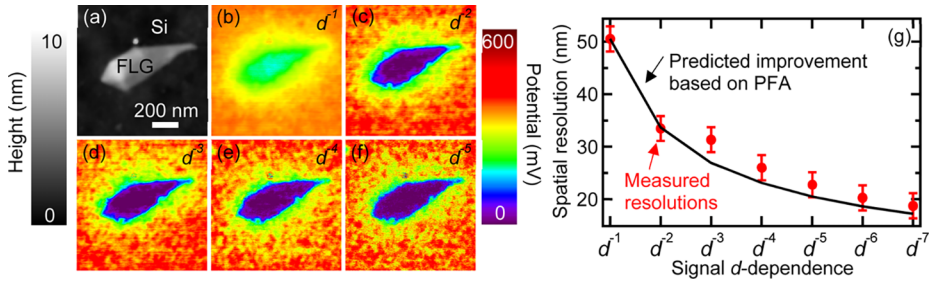

Figure 3. (a) Topography and (b−f) voltage scans of a flake of FLG on Si scanned with KPFM using successively larger values for the power-law dependence of the tip−sample separation d^{-n}, as noted in the upper right corner of each image. (g) Spatial resolution enhancement as a function of signal d-dependence obtained with HM-KPFM.

DOI: 10.1021/acsami.8b08097
ACS Appl. Mater. Interfaces 2018, 10, 28850−28859

and then average the potential as a function of its distance from the boundary at several points, each of which is fit to a hyperbolic tangent function[10] (Figure S4). As displayed in Figure 3g, the spatial resolution of the scans improves by increasing the d-dependence.

The dependence on n observed in the measured minimum detectable voltages, $V_{min}(n)$, of the HM-KPFM technique is consistent with our predictions about HM. Because $V_{min}(n) \propto 1/|F_{\omega_M \pm n\omega_T}|$, two predictions about how $V_{min}(n)$ scales with n can be drawn from eq 2. First, at a constant A_T, $V_{min}(n)$ increases by a constant proportion for each increase in n. Second, the increase is greater when the oscillation amplitude A_T is smaller relative to the average separation. Our measurements are consistent with both predictions of eq 2 (Figure 4). By comparing $V_{min}(n)$ for several n, we verify eq 2

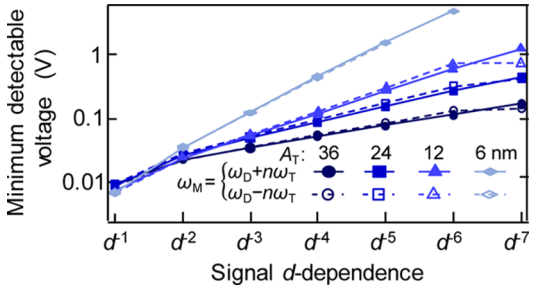

Figure 4. Minimum detectable voltage as a function of the signal d-dependence for a detection bandwidth of 200 Hz and V_{ac} = 1 V, measured for four different oscillation amplitudes A_T, for n = 0–6.

without needing to determine the closest approach, on which the predicted force is extremely sensitive and which requires an additional mechanically driven signal to estimate.[56]

One advantage of the HM technique is that the number of signals amplified by a single cantilever eigenmode is limited only by bandwidth. Therefore, we test the capability to amplify multiple signals with open-loop KPFM. Unlike closed-loop variants, open-loop KPFM relies on a force at twice the frequency of the applied ac voltage to generate a second signal to calibrate the primary KPFM signal.[47−49] Because no low-frequency bias voltage is applied, open-loop KPFM is ideal for scanning surfaces that are sensitive to a dc bias, for example, in exploring phenomena related to corrosion and in devices such as batteries.[20,49]

To implement open-loop HM-KPFM, we apply ac voltages to the cantilever at two different frequencies that are chosen so that the detected primary and the calibrating KPFM signals are separated by 1 kHz in the frequency space and centered on the second cantilever resonance, while the sample is grounded. The potential is then calculated by normalizing the primary KPFM signal by the calibrating signal. As shown in Figure 5, open-loop HM-KPFM provides a significant resolution improvement on a FLG/Si boundary for d-dependences from d^{-1} to d^{-3}. Here, the number of signals that can be amplified is constrained only by the total bandwidth of the eigenmode, the bandwidth required for each signal to avoid interference, and the number of lock-in amplifiers (LIAs) available. For cases where a large bandwidth is more important than sensitivity, multiple eigenmodes can be used to amplify the signals, though their relative sensitivities must be taken into account. Changes in the transfer function on approach lead to a 5% systematic overestimation of the potential contrast (see the Supporting Information and Figure S2).

Resolving Electrostatic Patch Potentials in Metallic Thin Films. A primary reason for the development of HM-KPFM is the need to improve the resolution of the electrostatic potential of a surface, particularly relevant for situations where the voltage heterogeneity is not directly correlated with topography. To demonstrate the utility of HM-KPFM for this application, we map the surface voltage of an Au film at distinct n (see Figure 6a–c). Substantial spatial variations in the V_{CPD} signal are detected. We compare how well the patch potentials are resolved when using different n by means of a potential autocorrelation function, which is the product of the measured voltages at two pixels in an AFM image, separated by a radial distance r, averaged over the entire scanned region.[27] With sufficiently high spatial resolution and a large scan size, the autocorrelation function is accurately determined. However, if the spatial resolution is too low, the autocorrelation function will vary with resolution (i.e., it will vary with n). Specifically, insufficient spatial resolution artificially decreases the autocorrelation function at the

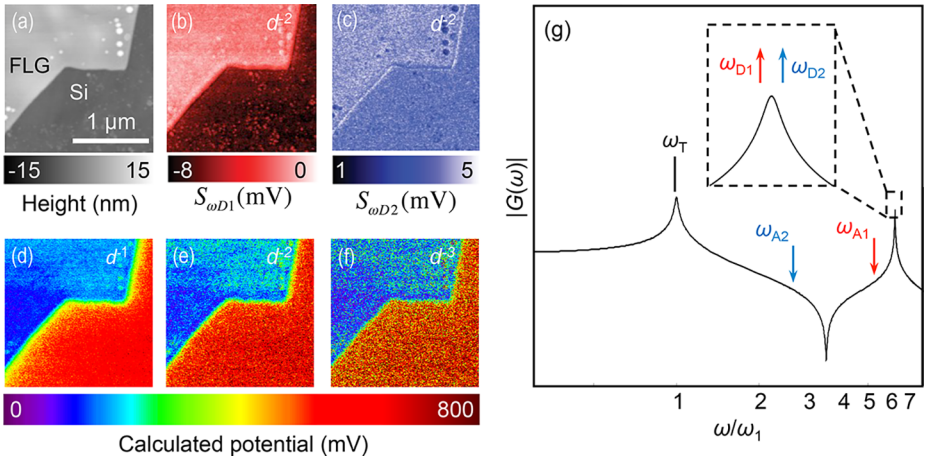

Figure 5. Open-loop HM-KPFM. (a) Topography of FLG on Si. (b) Primary KPFM signal and (c) calibrating signal. (d–f) Potential difference for n = 0–2 (corresponding to d^{-1} to d^{-3}) calculated from the ratio of (b) to (c). (g) Frequencies ω at which ac voltages are applied (ω_{A1} and ω_{A2}) and signals are detected (ω_{D1} and ω_{D2}) are superimposed on the cantilever transfer function for the n = 1 case. The "1" and "2" subscripts correspond to the primary and the normalizing KPFM signals, respectively.

DOI: 10.1021/acsami.8b08097
ACS Appl. Mater. Interfaces 2018, 10, 28850−28859

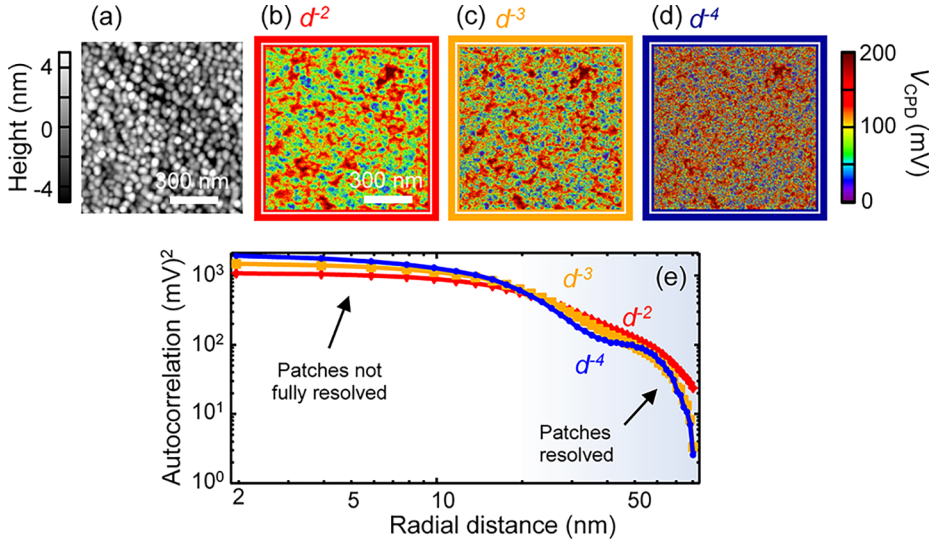

Figure 6. (a) Topography of a thin Au film showing various grain boundaries. (b–d) Surface potential of the film measured with HM-KPFM at three different resolutions. (e) Autocorrelation function used to characterize the patch potentials on the Au surface.

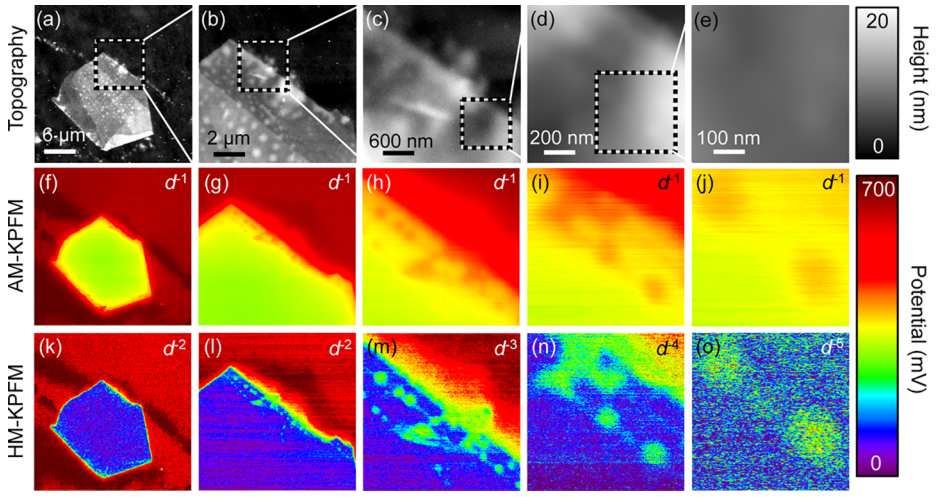

Figure 7. Demonstration of multiscale scanning through HM-KPFM. (a–e) AFM topography scans at the boundary between a FLG flake and a Si substrate. (f–j) AM-KPFM and (k–o) HM-KPFM performed on the same regions. The *d*-dependence of the signal used to acquire each scan is noted in the upper right corner.

shortest separations, while simultaneously increasing it for slightly larger separations. The ability of HM-KPFM to vary the spatial resolution permits one to test how well patches are being resolved (Figure 6).

By comparing the autocorrelation functions obtained with different n values, we determine that individual patches are resolved to <50 nm. To demonstrate the resolving power of this technique, the d-dependence of the KPFM signal used to measure the patches is increased from d^{-2} to d^{-4} across several scans of the Au surface (Figure 6d). For r > 50 nm, the autocorrelation function changes as the distance dependence is increased from d^{-2} and d^{-3}, suggesting that patches of this size have not yet been fully resolved. However, when transitioning from d^{-3} to d^{-4}, the autocorrelation functions remain similar, indicating that the patch potentials of that characteristic size are now resolved (with d^{-4}). For r < 20 nm, no value of n results in a convergence of the autocorrelation functions. Thus, the smallest patches that can be accurately resolved are between 20 and 50 nm.

AFM Measurements at Multiple Length Scales. Our HM technique enables the investigation of surfaces at multiple length scales, as demonstrated in Figure 7. When HM-KPFM is set to a low resolution, it can quickly scan a relatively large area because of its high voltage sensitivity. A region of interest, such as an interface, identified in the first scan, is subsequently scanned using HM with higher spatial resolution settings. To demonstrate the concept of multiscale scanning, we combine information about the overall shape of a flake of FLG (Figure 7a,f,k) with the information about the inhomogeneous potential at the edge of the flake/Si interface (Figure 7c,h,m). Each $(256)^2$ pixel scan requires the same time to complete (≈4.3 min).

Because boundaries and interfaces are critical to the functionality of nearly all nanoscale devices, we evaluate how much information HM contributes by combining scans of an entire FLG flake with better-resolved scans of its boundary with Si. As presented in Figure 7f,k, both of the $(30\ \mu m)^2$ scans show a homogeneous FLG flake on a Si substrate. At this magnification, a deconvolution procedure could readily

DOI: 10.1021/acsami.8b08097
ACS Appl. Mater. Interfaces 2018, 10, 28850–28859

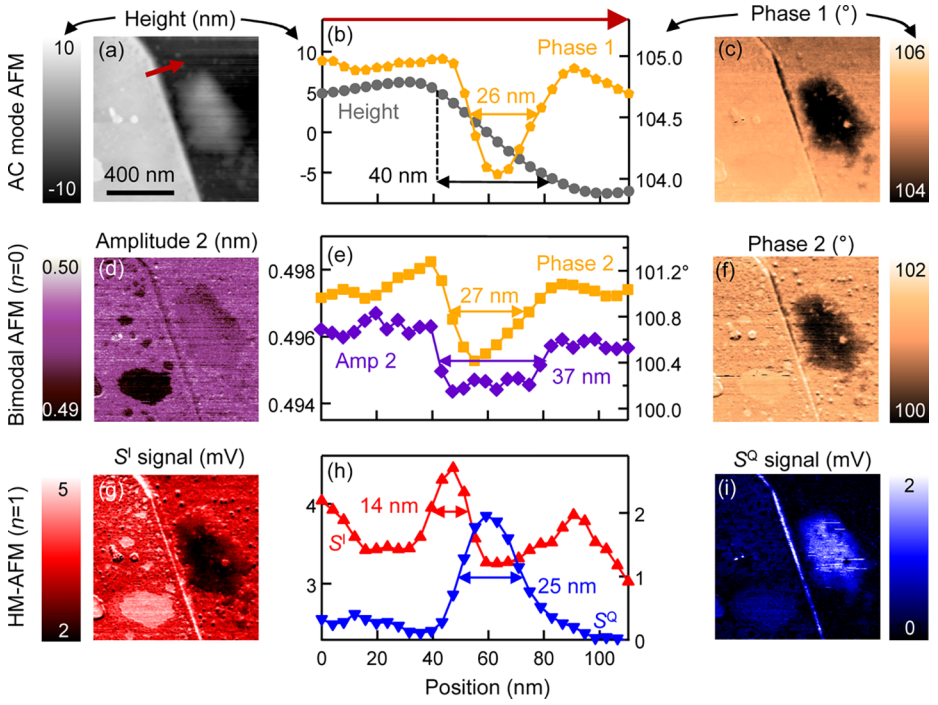

Figure 8. (a–c) Topography, line profile, and phase measured with ac mode AFM. (d–f) Phase, line profile, and amplitude at the second eigenmode, collected using bimodal AFM. (g–i) When the cantilever is also oscillated at $\omega_M = \omega_2 - \omega_T$ with an amplitude of ≈1.4 nm, in-phase (S^I) and quadrature (S^Q) components of the LIA at ω_2 are generated by the mixing of the oscillations at ω_T and ω_M. (b,e,h) Width of the contrast of the FLG edge along the red arrow in (a) is calculated for each of the signals.

determine the FLG/Si potential difference. Note that the potential contrast in the AM-KPFM image is smaller than that in the HM-KPFM because the stray capacitance of the cantilever artificially decreases the contrast in AM-KPFM.[8,10] The next scans (Figure 7g,l), each (10 μm)^2, show that the edge of the FLG is not uniform, but instead that there is a region of Si near the boundary at lower potential than the bulk, likely due to band bending,[57] as well as small regions of the FLG near the interface that have a higher potential than the bulk FLG. Note that while HM-KPFM resolves both sets of heterogeneities very well, in AM-AFM the many small subregions of the FLG blur together. In the (3 μm)^2 images shown in Figure 7h,m, HM-KPFM clearly resolves the substructure of the boundary, unlike AM-KPFM. In the (1 μm)^2 images, HM-KPFM resolves a few more line features in the potential of the FLG at about the noise level (Figure 7i,n). As expected, in the (0.5 μm)^2 images displayed in Figure 7j,o, which correspond to d^{-5}, the noise level is large enough to subsume any newly resolved features, and we have reached the resolving power of the method. Our strategy presents a framework to harness the benefits of both the high sensitivity and high-resolution settings of HM-KPFM, enabling the collection of information at several length scales with a single AFM probe in one experiment.

Actuation by Other Forces. Any tip–sample force that can be modulated can drive the HM technique. Recent experiments show that it is possible to use the sideband technique, from which HM is generalized, with magnetic and photoinduced forces as well as the electrostatic force.[44,45,58] Moreover, it is expected that other forces present at the nanoscale can be controlled as well, such as van der Waals/Casimir forces,[59,60] which may be useful for detecting impurities in metals.[61] The total tip–sample force can even be modulated by changing the tip–sample separation.

In this section, we borrow an actuation technique from van der Waals/Casimir force measurements to modulate the total tip–sample force.[62,63] In those measurements, sinusoidal motion of the sample position governs the total force. However, here we modulate the separation between the tip and the sample by shaking the cantilever instead of the sample because the piezo transfer function associated with sample motion is well-behaved only up to about 2 kHz. Because the AFM already detects the cantilever's displacement, the amplitude of the separation oscillation can be directly monitored and controlled. In addition, the direction of modulation can be controlled through the choice of actuated eigenmodes, which can be used to map in-plane forces.[53,64,65] As the separation changes, the total tip–sample force is itself modulated at ω_M. Mixing the force modulation at ω_M with motion at ω_T generates a force at ω_D. We call this method of actuation HM-AFM. There are other techniques that use a nonlinear tip–sample force to excite the cantilever at frequencies different from the driving ones,[51,66] but the HM method shows that the signal can be amplified by a resonance at ω_D as long as the $\omega_M = \omega_D \pm n\omega_T$ condition is satisfied. For sufficiently simple forces, the signals generated by conservative and dissipative interactions are separated by a 90° phase shift, as is used to separate the Casimir and hydrodynamic forces in precision measurements[62] (S^I and S^Q, respectively, see the Supporting Information). Note that n = 0 HM-AFM is equivalent to bimodal AFM, so we use that terminology.

FLG and the adhesive residue on Si (see Figure 8) are scanned using both n = 0 and n = 1. Because both the detection and the force modulation occur at the same frequency when using the n = 0 setting, the images are formed using the amplitude and phase of oscillation at ω_D, as commonly done in bimodal AFM.[50,51] We determine the reference phase for the n = 1 setting by positioning the probe

DOI: 10.1021/acsami.8b08097
ACS Appl. Mater. Interfaces 2018, 10, 28850–28859

Table 1. Cantilevers and Settings Used for Measurements

figure #	cantilever	$\omega_D/2\pi$ (kHz)	$\omega_T/2\pi$ (kHz)	harmonics n used (+/− for branches)	force	A_T/A_M (nm)	V_{ac} (V)
2	NSC35/Pt-C	738	115	0, −1, −2, −3	$F_{2\omega_A}$	25/-	5
3a−f	NSC35/Pt-C	160	161	0, +1, +2, +3, +4	F_{ω_A}	25/-	3
3g	NSC35/Pt-A	1194	188	0, +1, +2, +3, +4, +5, +6	F_{ω_A}	24/-	1
4	NSC35/Pt-A	1194	188	0, +1, +2, +3, +4, +5, +6, −1, −2, −3, −4, −5, −6	F_{ω_A}	6, 12, 24, 36/-	1
5	NSC35/Pt-C	775	122	0, −1, −2	F_{ω_A}, $F_{2\omega_A}$	21/-	1
6	NSC35/Pt-C	811	127	+1, +2, +3	F_{ω_A}	22/-	1
7	NSC35/Pt-C	119	120	0, +1, +2, +3, +4	F_{ω_A}	27/-	5
8	NSC35 Al BS-C	772	117	0, −1	F_{tot}	10/0.5	
S2	NSC35/Pt-C						
S3	CSC37/Pt-B	141	22	0, +1, +2, +3	F_{ω_A}	84/-	5
S4	NSC35/Pt-A	1194	188	0, +1, +2, +3, +4, +5, +6	F_{ω_A}	24/-	1

over the bare Si surface and adjusting it so that the entire signal falls in the S^I channel (assuming that the force is mostly conservative when measuring on bare Si). In both bimodal AFM and HM-AFM, there is a contrast between the adhesive and Si and among subregions of the FLG, most likely due to either adsorbates or subsurface molecules.[67]

The S^Q signal is strongest above the adhesive and at the edge of the FLG, where the adhesive is likely present, which supports the prediction that it measures dissipative forces. Notably, line noise is present only in the S^Q image and there it is only present above the adhesive. The line noise is likely due to a meniscus forming between the tip and the adhesive or a molecule briefly adhering to the tip. The absence of the line noise from the S^I image further attests to the separation of the conservative and dissipative forces.

We choose the FLG/Si boundary to characterize the resolution of each signal because it correlates with a sharp topographical feature, whereas the other boundaries in the image are less well-defined. The width of the signals plotted in Figure 8b,e,h shows that HM-AFM does resolve the heterogeneity of the boundary more clearly than either bimodal AFM or basic ac mode AFM. The S^I signal shows a 14 nm wide region with a relatively large conservative force signal, most likely because of adsorbates at the FLG edge.[68] The S^Q signal resolution (Figure 8i) is comparable to phase in each of the two other modes, which is consistent with the fact that phase shifts typically correlate with changes in dissipation.[69] The width of the edge in the amplitude 2 signal of bimodal AFM, 37 nm, is almost as large as the sum of the widths calculated from the two HM-AFM data channels. By separating conservative and dissipative forces, HM-AFM reveals heterogeneity in regions of the boundary that appeared uniform with bimodal AFM. Although the heterogeneous nature of the forces contributing to the total force complicates a general definition of resolution, developing a procedure to convert the signal to a force, as has been done for other AFM techniques, should clarify what additional features can be resolved with HM-AFM by using larger n. The scans in Figure 8 demonstrate that the HM technique is sufficiently general to incorporate forces other than the electrostatic force.

CONCLUSIONS

We showed that HM in AFM improves spatial resolution by changing the d-dependence of the signal generated by tip−sample forces. Our measurements demonstrated that the power-law dependence of the signal generated by the electrostatic force can be tailored from d^{-1} to d^{-4}. The change in the d-dependence leads to a factor of two improvement to the 10−90 spatial resolution. We verified the ability of HM to amplify multiple signals at once by open-loop KPFM, and the technique was used to characterize the distribution of patch potentials on an Au surface. Because the HM technique is generalizable to forces other than the electrostatic force, we foresee it enabling better resolution control with a variety of modulated tip−sample forces critical to nanoscience, such as optical forces for spectroscopy and plasmonic imaging, magnetic force for data storage, and van der Waals forces.

METHODS

Kelvin Probe Force Microscopy. For the KPFM measurements, platinum-coated HQ: NSC35/Pt probes (MikroMasch, USA) are used in a Cypher atomic force microscope (Asylum Research). The topographical oscillation is excited photothermally for the data presented in Figures 3 and 4 and piezoelectrically otherwise. The HM technique is implemented with the topographical control oscillation frequency $\omega_T \approx \omega_1$ slightly detuned above resonance to remain in attractive ac mode[70] for all measurements (Table 1). The detection frequency is varied between the second eigenmode $\omega_D = \omega_2$ for the data presented in Figures 2, 3g, 4−6, and 8, whereas the first eigenmode amplifies the signal for the data in Figures 3a−f and 7 in order to enhance the sensitivity at the price of speed and stability ($\omega_D = \omega_1 - \Delta\omega$, with $\Delta\omega < 1$ kHz and $\omega_M = \omega_D + n\omega_T$). The F_{ω_A} electrostatic force (for an ac voltage applied at ω) is used to drive the HM signal for figures except 2, 5, and 8. In Figure 2, the $F_{2\omega_A}$ force is used, and in Figure 5, both the F_{ω_A} and $F_{2\omega_A}$ forces are used. Figure 8 used piezoelectric rather than electrostatic actuation of the HM signal. The relationship between the F_{ω_A} and $F_{2\omega_A}$ portions of the electrostatic force is discussed in the Supporting Information.

In Figure 3, the 10−90 resolution is calculated by fitting the potential as a function of its distance to a boundary to a hyperbolic tangent function. The minimum detectable voltage is measured by sweeping V_K from −1.5 to 1.5 V, across the force minimum, with 20 different relative phases settings between −180° and 180° on LIA, each collected for 1 s. The minimizing voltage is then N/ξ, where N is the measured noise (in mV) in a 200 Hz bandwidth and ξ is the KPFM sensitivity.[10] Three LIAs are used: one controls the topography loop, one generates the voltages, and one detects the voltage signals.[10,22] For the HM-AFM measurement, one LIA drives the cantilever and another detects its oscillation. The LIAs are all synchronized through an 80 MHz internal clock. For HM-KPFM, the relative phase of the detection LIA is set by varying its phase so that the electrostatic signal is completely in the in-phase component. For HM-AFM, the phase is set so that the whole signal is in the S^I channel when the tip is above bare Si. The KPFM images are 0th order flattened to remove line noise.

DOI: 10.1021/acsami.8b08097
ACS Appl. Mater. Interfaces 2018, 10, 28850−28859

The Au surface is prepared by depositing 100 nm of Au with a 5 nm Cr sticking layer on a Si wafer (Figures 2 and 6). The FLG sample is fabricated by exfoliating a piece of highly ordered pyrolytic graphite onto boron-doped Si (15−25 Ωcm, Virginia Semiconductor).

■ ASSOCIATED CONTENT

Supporting Information

The Supporting Information is available free of charge on the ACS Publications website at DOI: 10.1021/acsami.8b08097.

Spatial resolution from separation dependence, separation dependence of electrostatic force signal, force modulation by cantilever oscillation, effects of amplitude on resolution and sensitivity, damping of the cantilever near a surface, and reliable imaging tactics (PDF)

■ AUTHOR INFORMATION

Corresponding Author

*E-mail: jnmunday@umd.edu.

ORCID

Joseph L. Garrett: 0000-0001-8265-0661

Marina S. Leite: 0000-0003-4888-8195

Jeremy N. Munday: 0000-0002-0881-9876

Author Contributions

J.L.G. performed experiments and calculations. All authors contributed to the analysis of data and writing of the manuscript.

Notes

The authors declare no competing financial interest.

■ ACKNOWLEDGMENTS

The authors acknowledge partial funding support from the Office of Naval Research under grant no. N00014-16-1-2540, the National Science Foundation (ECCS, award 16-10833), and a University of Maryland Tier 1 Award. The authors also thank D. A. T. Somers and E. M. Tennyson for comments and fruitful discussion and acknowledge the support of the Maryland NanoCenter and its FabLab.

■ ABBREVIATIONS

HM, harmonic mixing; AFM, atomic force microscopy; KPFM, Kelvin probe force microscopy; PFA, proximity force approximation

■ REFERENCES

(1) Binnig, G.; Quate, C. F.; Gerber, C. Atomic Force Microscope. *Phys. Rev. Lett.* **1986**, *56*, 930−933.

(2) Bonnell, D. A.; Basov, D. N.; Bode, M.; Diebold, U.; Kalinin, S. V.; Madhavan, V.; Novotny, L.; Salmeron, M.; Schwarz, U. D.; Weiss, P. S. Imaging Physical Phenomena with Local Probes: From Electrons to Photons. *Rev. Mod. Phys.* **2012**, *84*, 1343−1381.

(3) Kalinin, S. V.; Strelcov, E.; Belianinov, A.; Somnath, S.; Vasudevan, R. K.; Lingerfelt, E. J.; Archibald, R. K.; Chen, C.; Proksch, R.; Laanait, N.; Jesse, S. Big, Deep, and Smart Data in Scanning Probe Microscopy. *ACS Nano* **2016**, *10*, 9068−9086.

(4) Tennyson, E. M.; Gong, C.; Leite, M. S. Imaging Energy Harvesting and Storage Systems at the Nanoscale. *ACS Energy Lett.* **2017**, *2*, 2761−2777.

(5) Weaver, J. M. R.; Abraham, D. W. High Resolution Atomic Force Microscopy Potentiometry. *J. Vac. Sci. Technol., B: Microelectron. Nanometer Struct.–Process., Meas., Phenom.* **1991**, *9*, 1559.

(6) Nonnenmacher, M.; O'Boyle, M. P.; Wickramasinghe, H. K. Kelvin Probe Force Microscopy. *Appl. Phys. Lett.* **1991**, *58*, 2921−2923.

(7) Kitamura, S.; Iwatsuki, M. High-Resolution Imaging of Contact Potential Difference with Ultrahigh Vacuum Noncontact Atomic Force Microscope. *Appl. Phys. Lett.* **1998**, *72*, 3154−3156.

(8) Ma, Z. M.; Kou, L.; Naitoh, Y.; Li, Y. J.; Sugawara, Y. The Stray Capacitance Effect in Kelvin Probe Force Microscopy Using FM, AM and Heterodyne AM Modes. *Nanotechnology* **2013**, *24*, 225701.

(9) Collins, L.; Jesse, S.; Kilpatrick, J. I.; Tselev, A.; Varenyk, O.; Okatan, M. B.; Weber, S. A. L.; Kumar, A.; Balke, N.; Kalinin, S. V.; Rodriguez, B. J. Probing Charge Screening Dynamics and Electrochemical Processes at the Solid-Liquid Interface with Electrochemical Force Microscopy. *Nat. Commun.* **2014**, *5*, 3871.

(10) Garrett, J. L.; Munday, J. N. Fast, High-Resolution Surface Potential Measurements in Air with Heterodyne Kelvin Probe Force Microscopy. *Nanotechnology* **2016**, *27*, 245705.

(11) Collins, L.; Ahmadi, M.; Wu, T.; Hu, B.; Kalinin, S. V.; Jesse, S. Breaking the Time Barrier in Kelvin Probe Force Microscopy: Fast Free Force Reconstruction Using the G-Mode Platform. *ACS Nano* **2017**, *11*, 8717−8729.

(12) Dwyer, R. P.; Smieska, L. M.; Tirmzi, A. M.; Marohn, J. A. Vector Electric Field Measurement via Position-Modulated Kelvin Probe Force Microscopy. *Appl. Phys. Lett.* **2017**, *111*, 173106.

(13) Sinensky, A. K.; Belcher, A. M. Label-Free and High-Resolution Protein/DNA Nanoarray Analysis Using Kelvin Probe Force Microscopy. *Nat. Nanotechnol.* **2007**, *2*, 653−659.

(14) Ida, S.; Takashiba, A.; Koga, S.; Hagiwara, H.; Ishihara, T. Potential Gradient and Photocatalytic Activity of an Ultrathin p-n Junction Surface Prepared with Two-Dimensional Semiconducting Nanocrystals. *J. Am. Chem. Soc.* **2014**, *136*, 1872−1878.

(15) Almadori, Y.; Bendiab, N.; Grévin, B. Multimodal Kelvin Probe Force Microscopy Investigations of a Photovoltaic WSe2/MoS2 Type-II Interface. *ACS Appl. Mater. Interfaces* **2018**, *10*, 1363−1373.

(16) Rogero, C.; Pickup, D. F.; Colchero, J.; Azaceta, E.; Tena-Zaera, R.; Palacios-Lidón, E. Nanophotoactivity of Porphyrin Functionalized Polycrystalline ZnO Films. *ACS Appl. Mater. Interfaces* **2016**, *8*, 16783−16790.

(17) Palacios-Lidón, E.; Henry, C. R.; Barth, C. Kelvin Probe Force Microscopy in Surface Chemistry: Reactivity of Pd Nanoparticles on Highly Oriented Pirolytic Graphite. *ACS Catal.* **2014**, *4*, 1838−1844.

(18) Tennyson, E. M.; Garrett, J. L.; Frantz, J. A.; Myers, J. D.; Bekele, R. Y.; Sanghera, J. S.; Munday, J. N.; Leite, M. S. Nanoimaging of Open-Circuit Voltage in Photovoltaic Devices. *Adv. Energy Mater.* **2015**, *5*, 1501142.

(19) Bergmann, V. W.; Guo, Y.; Tanaka, H.; Hermes, I. M.; Li, D.; Klasen, A.; Bretschneider, S. A.; Nakamura, E.; Berger, R.; Weber, S. A. L. Local Time-Dependent Charging in a Perovskite Solar Cell. *ACS Appl. Mater. Interfaces* **2016**, *8*, 19402−19409.

(20) Masuda, H.; Ishida, N.; Ogata, Y.; Ito, D.; Fujita, D. Internal Potential Mapping of Charged Solid-State-Lithium Ion Batteries Using in Situ Kelvin Probe Force Microscopy. *Nanoscale* **2017**, *9*, 893−898.

(21) Zhu, J.; Pang, S.; Dittrich, T.; Gao, Y.; Nie, W.; Cui, J.; Chen, R.; An, H.; Fan, F.; Li, C. Visualizing the Nano Cocatalyst Aligned Electric Fields on Single Photocatalyst Particles. *Nano Lett.* **2017**, *17*, 6735−6741.

(22) Garrett, J. L.; Tennyson, E. M.; Hu, M.; Huang, J.; Munday, J. N.; Leite, M. S. Real-Time Nanoscale Open-Circuit Voltage Dynamics of Perovskite Solar Cells. *Nano Lett.* **2017**, *17*, 2554−2560.

(23) Konečný, M.; Bartošík, M.; Mach, J.; Švarc, V.; Nezval, D.; Piastek, J.; Procházka, P.; Cahlík, A.; Šikola, T. Kelvin Probe Force Microscopy and Calculation of Charge Transport in a Graphene/Silicon Dioxide System at Different Relative Humidity. *ACS Appl. Mater. Interfaces* **2018**, *10*, 11987−11994.

(24) Will, J.; Hou, Y.; Scheiner, S.; Pinkert, U.; Hermes, I. M.; Weber, S. A. L.; Hirsch, A.; Halik, M.; Brabec, C.; Unruh, T. Evidence of Tailoring the Interfacial Chemical Composition in Normal Structure Hybrid Organohalide Perovskites by a Self-Assembled Monolayer. *ACS Appl. Mater. Interfaces* **2018**, *10*, 5511−5518.

(25) Strassburg, E.; Boag, A.; Rosenwaks, Y. Reconstruction of Electrostatic Force Microscopy Images. *Rev. Sci. Instrum.* **2005**, *76*, 083705.
(26) Machleidt, T.; Sparrer, E.; Kapusi, D.; Franke, K.-H. Deconvolution of Kelvin probe force microscopy measurements-methodology and application. *Meas. Sci. Technol.* **2009**, *20*, 084017.
(27) Speake, C. C.; Trenkel, C. Forces between Conducting Surfaces Due to Spatial Variations of Surface Potential. *Phys. Rev. Lett.* **2003**, *90*, 160403.
(28) Pu, Y.; Neufeld, D. D.; Dunning, F. B. Ionization of Rydberg Atoms at Metallic Surfaces: Influence of Stray Fields. *Phys. Rev. A: At., Mol., Opt. Phys.* **2010**, *81*, 042904.
(29) Baytekin, H. T.; Patashinski, A. Z.; Branicki, M.; Baytekin, B.; Soh, S.; Grzybowski, B. A. The Mosaic of Surface Charge in Contact Electrification. *Science* **2011**, *333*, 308−312.
(30) Antonucci, F.; Cavalleri, A.; Dolesi, R.; Hueller, M.; Nicolodi, D.; Tu, H. B.; Vitale, S.; Weber, W. J. Interaction between Stray Electrostatic Fields and a Charged Free-Falling Test Mass. *Phys. Rev. Lett.* **2012**, *108*, 181101.
(31) Burson, K. M.; Cullen, W. G.; Adam, S.; Dean, C. R.; Watanabe, K.; Taniguchi, T.; Kim, P.; Fuhrer, M. S. Direct Imaging of Charged Impurity Density in Common Graphene Substrates. *Nano Lett.* **2013**, *13*, 3576−3580.
(32) Behunin, R.; Dalvit, D. A.; Decca, R.; Genet, C.; Jung, I.; Lambrecht, A.; Liscio, A.; López, D.; Reynaud, S.; Schnoering, G.; Voisin, G.; Zeng, Y. Kelvin Probe Force Microscopy of Metallic Surfaces Used in Casimir Force Measurements. *Phys. Rev. A: At., Mol., Opt. Phys.* **2014**, *90*, 062115.
(33) Garrett, J. L.; Somers, D.; Munday, J. N. The Effect of Patch Potentials in Casimir Force Measurements Determined by Heterodyne Kelvin Probe Force Microscopy. *J. Phys.: Condens. Matter* **2015**, *27*, 214012.
(34) Ortuño, M.; Escasain, E.; Lopez-Elvira, E.; Somoza, A. M.; Colchero, J.; Palacios-Lidon, E. Conducting Polymers as Electron Glasses: Surface Charge Domains and Slow Relaxation. *Sci. Rep.* **2016**, *6*, 21647.
(35) Giessibl, F. J. Advances in Atomic Force Microscopy. *Rev. Mod. Phys.* **2003**, *75*, 949−983.
(36) Giessibl, F. J.; Bielefeldt, H.; Hembacher, S.; Mannhart, J. Calculation of the Optimal Imaging Parameters for Frequency Modulation Atomic Force Microscopy. *Appl. Surf. Sci.* **1999**, *140*, 352−357.
(37) Palacios-Lidón, E.; Pérez-García, B.; Colchero, J. Enhancing Dynamic Scanning Force Microscopy in Air: As Close as Possible. *Nanotechnology* **2009**, *20*, 085707.
(38) Hutter, J. L.; Bechhoefer, J. Manipulation of van der Waals forces to improve image resolution in atomic-force microscopy. *J. Appl. Phys.* **1993**, *73*, 4123−4129.
(39) Kumar, S.; Cartron, M. L.; Mullin, N.; Qian, P.; Leggett, G. J.; Hunter, C. N.; Hobbs, J. K. Direct Imaging of Protein Organization in an Intact Bacterial Organelle Using High-Resolution Atomic Force Microscopy. *ACS Nano* **2017**, *11*, 126−133.
(40) Gross, L.; Mohn, F.; Moll, N.; Liljeroth, P.; Meyer, G. The Chemical Structure of a Molecule Resolved by Atomic Force Microscopy. *Science* **2009**, *325*, 1110−1114.
(41) Wagner, C.; Green, M. F. B.; Leinen, P.; Deilmann, T.; Krüger, P.; Rohlfing, M.; Temirov, R.; Tautz, F. S. Scanning Quantum Dot Microscopy. *Phys. Rev. Lett.* **2015**, *115*, 026101.
(42) Schuler, B.; Liu, S.-X.; Geng, Y.; Decurtins, S.; Meyer, G.; Gross, L. Contrast Formation in Kelvin Probe Force Microscopy of Single π-Conjugated Molecules. *Nano Lett.* **2014**, *14*, 3342−3346.
(43) Zerweck, U.; Loppacher, C.; Otto, T.; Grafström, S.; Eng, L. M. Accuracy and Resolution Limits of Kelvin Probe Force Microscopy. *Phys. Rev. B: Condens. Matter Mater. Phys.* **2005**, *71*, 125424.
(44) Arima, E.; Naitoh, Y.; Li, Y. J.; Yoshimura, S.; Saito, H.; Nomura, H.; Nakatani, R.; Sugawara, Y. Magnetic Force Microscopy Using Tip Magnetization Modulated by Ferromagnetic Resonance. *Nanotechnology* **2015**, *26*, 125701.
(45) Jahng, J.; Fishman, D. A.; Park, S.; Nowak, D. B.; Morrison, W. A.; Wickramasinghe, H. K.; Potma, E. O. Linear and Nonlinear Optical Spectroscopy at the Nanoscale with Photoinduced Force Microscopy. *Acc. Chem. Res.* **2015**, *48*, 2671−2679.
(46) Giessibl, F. J. Higher-Harmonic Atomic Force Microscopy. *Surf. Interface Anal.* **2006**, *38*, 1696−1701.
(47) Takeuchi, O.; Ohrai, Y.; Yoshida, S.; Shigekawa, H. Kelvin Probe Force Microscopy without Bias-Voltage Feedback. *Jpn. J. Appl. Phys.* **2007**, *46*, 5626−5630.
(48) Collins, L.; Kilpatrick, J. I.; Weber, S. A. L.; Tselev, A.; Vlassiouk, I. V.; Ivanov, I. N.; Jesse, S.; Kalinin, S. V.; Rodriguez, B. J. Open Loop Kelvin Probe Force Microscopy with Single and Multi-Frequency Excitation. *Nanotechnology* **2013**, *24*, 475702.
(49) Honbo, K.; Ogata, S.; Kitagawa, T.; Okamoto, T.; Kobayashi, N.; Sugimoto, I.; Shima, S.; Fukunaga, A.; Takatoh, C.; Fukuma, T. Visualizing Nanoscale Distribution of Corrosion Cells by Open-Loop Electric Potential Microscopy. *ACS Nano* **2016**, *10*, 2575−2583.
(50) Herruzo, E. T.; Perrino, A. P.; Garcia, R. Fast Nanomechanical Spectroscopy of Soft Matter. *Nat. Commun.* **2014**, *5*, 3126.
(51) Forchheimer, D.; Forchheimer, R.; Haviland, D. B. Improving Image Contrast and Material Discrimination with Nonlinear Response in Bimodal Atomic Force Microscopy. *Nat. Commun.* **2015**, *6*, 6270.
(52) Chawla, G.; Solares, S. D. Mapping of Conservative and Dissipative Interactions in Bimodal Atomic Force Microscopy Using Open-Loop and Phase-Locked-Loop Control of the Higher Eigenmode. *Appl. Phys. Lett.* **2011**, *99*, 074103.
(53) Garrett, J. L.; Krayer, L. J.; Palm, K. J.; Munday, J. N. Effect of Lateral Tip Motion on Multifrequency Atomic Force Microscopy. *Appl. Phys. Lett.* **2017**, *111*, 043105.
(54) Santos, S.; Guang, L.; Souier, T.; Gadelrab, K.; Chiesa, M.; Thomson, N. H. A Method to Provide Rapid in Situ Determination of Tip Radius in Dynamic Atomic Force Microscopy. *Rev. Sci. Instrum.* **2012**, *83*, 043707.
(55) Bakhti, S.; Destouches, N.; Hubert, C.; Reynaud, S.; Vocanson, F.; Ondarçuhu, T.; Epicier, T. Growth of Single Gold Nanofilaments at the Apex of Conductive Atomic Force Microscope Tips. *Nanoscale* **2016**, *8*, 7496−7500.
(56) Lai, C.-Y.; Perri, S.; Santos, S.; Garcia, R.; Chiesa, M. Rapid Quantitative Chemical Mapping of Surfaces with Sub-2 Nm Resolution. *Nanoscale* **2016**, *8*, 9688−9694.
(57) Glatzel, T.; Sadewasser, S.; Shikler, R.; Rosenwaks, Y.; Lux-Steiner, M. C. Kelvin probe force microscopy on III-V semiconductors: the effect of surface defects on the local work function. *Mater. Sci. Eng., B* **2003**, *102*, 138−142.
(58) Gu, K. L.; Zhou, Y.; Morrison, W. A.; Park, K.; Park, S.; Bao, Z. Nanoscale Domain Imaging of All-Polymer Organic Solar Cells by Photo-Induced Force Microscopy. *ACS Nano* **2018**, *12*, 1473−1481.
(59) Torricelli, G.; van Zwol, P. J.; Shpak, O.; Binns, C.; Palasantzas, G.; Kooi, B. J.; Svetovoy, V. B.; Wuttig, M. Switching Casimir Forces with Phase-Change Materials. *Phys. Rev. A: At., Mol., Opt. Phys.* **2010**, *82*, 010101.
(60) Allocca, A. A.; Wilson, J. H.; Galitski, V. Nonanalytic Behavior of the Casimir Force across a Lifshitz Transition in a Spin-Orbit-Coupled Material. *Phys. Rev. B: Condens. Matter Mater. Phys.* **2014**, *90*, 075420.
(61) Cherroret, N.; Crépin, P.-P.; Guérout, R.; Lambrecht, A.; Reynaud, S. Casimir-Polder Force Fluctuations as Spatial Probes of Dissipation in Metals. *Europhys. Lett.* **2017**, *117*, 63001.
(62) de Man, S.; Heeck, K.; Iannuzzi, D. Halving the Casimir Force with Conductive Oxides: Experimental Details. *Phys. Rev. A: At., Mol., Opt. Phys.* **2010**, *82*, 062512.
(63) Garrett, J. L.; Somers, D. A. T.; Munday, J. N. Measurement of the Casimir Force between Two Spheres. *Phys. Rev. Lett.* **2018**, *120*, 040401.
(64) Marcus, M. S.; Carpick, R. W.; Sasaki, D. Y.; Eriksson, M. A. Material Anisotropy Revealed by Phase Contrast in Intermittent Contact Atomic Force Microscopy. *Phys. Rev. Lett.* **2002**, *88*, 226103.

DOI: 10.1021/acsami.8b08097
ACS Appl. Mater. Interfaces 2018, 10, 28850−28859

(65) Reiche, C. F.; Vock, S.; Neu, V.; Schultz, L.; Büchner, B.; Mühl, T. Bidirectional Quantitative Force Gradient Microscopy. *New J. Phys.* **2015**, *17*, 013014.
(66) Lai, C.-Y.; Barcons, V.; Santos, S.; Chiesa, M. Periodicity in Bimodal Atomic Force Microscopy. *J. Appl. Phys.* **2015**, *118*, 044905.
(67) Geim, A. K. Graphene: Status and Prospects. *Science* **2009**, *324*, 1530−1534.
(68) Svatek, S. A.; Scott, O. R.; Rivett, J. P. H.; Wright, K.; Baldoni, M.; Bichoutskaia, E.; Taniguchi, T.; Watanabe, K.; Marsden, A. J.; Wilson, N. R.; Beton, P. H. Adsorbate-Induced Curvature and Stiffening of Graphene. *Nano Lett.* **2015**, *15*, 159−164.
(69) Cleveland, J. P.; Anczykowski, B.; Schmid, A. E.; Elings, V. B. Energy Dissipation in Tapping-Mode Atomic Force Microscopy. *Appl. Phys. Lett.* **1998**, *72*, 2613−2615.
(70) García, R.; San Paulo, A. Attractive and Repulsive Tip-Sample Interaction Regimes in Tapping-Mode Atomic Force Microscopy. *Phys. Rev. B: Condens. Matter Mater. Phys.* **1999**, *60*, 4961−4967.

DOI: 10.1021/acsami.8b08097
ACS Appl. Mater. Interfaces 2018, 10, 28850−28859